

A benchmark dataset of diurnal- and seasonal-scale radiation, heat and CO₂ fluxes in a typical East Asian monsoon region

Zexia Duan^{1#}, Zhiqiu Gao^{1,3#}, Qing Xu², Shaohui Zhou¹, Kai Qin^{2*}, Yuanjian Yang^{1*}

¹Climate and Weather Disasters Collaborative Innovation Center, Key Laboratory for Aerosol-Cloud-Precipitation of China Meteorological Administration, School of Atmospheric Physics, Nanjing University of Information Science and Technology, Nanjing, 210044, China

²Jiangsu Key Laboratory of Coal-Based Greenhouse Gas Control and Utilization, School of Environment and Spatial Informatics, China University of Mining and Technology, Xuzhou, 221116, China

³State Key Laboratory of Atmospheric Boundary Layer Physics and Atmospheric Chemistry, Institute of Atmospheric Physics, Chinese Academy of Sciences, Beijing, 100029, China

* Correspondence to: Yuanjian Yang (yyj1985@nuist.edu.cn) and Kai Qin (qinkai@cumt.edu.cn)

The authors contributed equally

Abstract A benchmark dataset of radiation, heat and CO₂ fluxes is crucial to land–atmosphere interaction research. Due to the rapid urbanization and the development of agriculture, land–atmosphere interaction process over the Yangtze River Delta (YRD) of China, which is the typical East Asian monsoon region, is becoming various and complex. To understand the effects of various land cover changes on land–atmosphere interaction in this region, a comprehensive long-term (2011–2019) in situ observation including 30-min-resolution meteorological variables (air temperature, humidity, pressure, wind speed, and wind direction), surface radiative flux, turbulent heat flux, and CO₂ flux was conducted at four sites with two typical surface types (i.e., croplands and suburbs) in the YRD. The dataset analyses showed that all four radiation components, latent heat flux, sensible heat flux, soil heat flux, and CO₂ fluxes varied seasonally and diurnally at four sites. Surface energy fluxes exhibited great differences among the four sites. On an annual basis, for two cropland sites, the dominant consumer of net radiation was latent heat flux. While for two suburb sites, latent heating dominated from April to November, whereas sensible heating dominated the other months. Our present work provides convincing evidences that the dataset has potentials for multiple research fields, including studying land–atmosphere interaction, improving the boundary-layer parameterization schemes, evaluating remote sensing algorithms, and developing climate models in the typical East Asian monsoon region.

The dataset is publicly available at <https://doi.org/10.5281/zenodo.6552301>, last access: 10 May 2022 (Duan et al., 2022).

1 Introduction

Land–atmosphere interaction processes, which control the surface–atmosphere exchanges of water, energy and atmospheric carbon dioxide (CO₂) across the atmospheric boundary layer, play a key role in ecosystem processes, hydrologic and biogeochemical cycles, and even in weather and climate (You et al., 2017; Yang et al., 2019). Previous studies showed that climate simulations were especially sensitive to seasonal and diurnal variations in the surface energy partitioning of available energy into sensible (H) and latent heat (λE) fluxes in numerical models (Gao et al., 2004), where considerable

uncertainties still remain in the land–surface parameters (Sun et al., 2013). These parameters' representation were not 35 optimal, indicated by validation against in situ observations (Cuntz et al., 2016). Thus, a comprehensive and accurate in situ eddy covariance (EC) flux measurement is essential to deepen the understanding of the land–atmosphere dynamics (Rao and Reddy, 2019).

The EC technique can derive direct observation of the land–atmosphere carbon, water, and energy fluxes exchanges, and is regarded as the best and the most trustworthy measurement of turbulent fluxes (Baldocchi, 2003). With the 40 development of the EC tool, there are more than 500 flux towers distributed in various climate zones (Lee et al., 2020; Kang and Cho, 2021). Under the same climate regions, the radiation budget and energy partitioning were mainly modulated by the surface properties (e.g., albedo and roughness length) and subsequently influenced air/surface temperature, humidity, and precipitation (Feddeema et al., 2005; Jin and Roy, 2005; Li and Wang, 2019). For example, aerodynamically rougher and 45 optically darker oak savanna absorbed more radiation and had higher H and air temperature than the aerodynamically smoother and optically brighter annual grassland, although both of them co-existed in semi-arid regions (Baldocchi and Ma, 2013). In the monsoon region, the land cover shifted from vegetation to bare soil in the Tibetan Plateau and Inner Mongolia, which not only modified the local thermal and hydrological behavior but also weakened East Asian summer monsoon circulation and precipitation (Li and Xue, 2010). Although some researchers have explored the roles of land surface 50 processes in the monsoon system (Xue et al., 2004), studies of field observations remain uncertain in the East Asian monsoon region (Bi et al., 2007), especially in the Yangtze River Delta (YRD) in the eastern China.

The YRD (114° – 122° E and 26° – 34° N), located in the typical East Asian monsoon region, is one of the most developed regions in China (Yang et al., 2020a; Zhang et al., 2021; Chen et al., 2022). It occupies only 2.2 % area of China, but represents about 16 % of China's total population (Huang et al., 2021) and contributes approximately 18.5 % of China's Gross Domestic Product in 2014 (Hu et al., 2018). Land cover types in the YRD are diverse, dominated by cropland, built-up 55 areas and mountainous areas (mostly forests and grasslands) across the northern, central, and southern of the YRD, respectively (Figure 1). Recently, the land cover is more complex in this area as it experienced rapid urbanization, industrialization, and agricultural development (Guo et al., 2016). The extensive urbanization increased H and CO_2 emissions, weakened the net surface long-wave radiation, as well as enhanced surface thermal heating to the atmosphere in this region (Chen and Zhang, 2013; Chen et al., 2016a). These alterations modified the urban surface energy budget and the 60 boundary layer structure (Wang et al., 2020; Yang et al., 2020b), resulting in distinct urban climate effects (e.g., urban heat island, enhanced heat waves, and flooding, Yang and Wang, 2014; Li et al., 2015). Meanwhile, large-scale vegetation degradation and agricultural activities, e.g., the frequent rotation of crop production with several dry–wet cycles in the northern of YRD, modulated the hydrological processes and subsequently affected the regional climate and East Asian monsoon circulation (Chen et al., 2016a). Thus, it is important to clarify the land–atmosphere interaction over the typical 65 surface types in the YRD.

In the past few years, some atmospheric field experiments have been conducted over various land surface types [e.g., croplands (Ge et al., 2018; Dai et al., 2019; Duan et al., 2021a) and urban areas (Ao et al., 2016; Wei et al., 2020)] to examine the temporal and spatial characteristics of the energy balance and greenhouse gases in the YRD. Nevertheless, integrated measurements from field stations in the YRD are still not openly shared, or only very limited data during a 70 specified observation period can be accessed. Although China Meteorological Data Service Center (<http://data.cma.cn/en>, last access: 30 April 2022) has provided some meteorological data in recent years, EC sensors have not been commonly equipped in those meteorological stations, making it difficult to obtain heat and CO₂ flux data at some specific places or periods (Flerchinger et al., 2009). To improve the knowledge of energy partitioning and CO₂ exchange over the typical land 75 surface in the YRD and to find out the strongest climate signals from surface energy components, a long-term (2011–2019) and continuous integrated observational dataset of land–atmosphere interaction with a high temporal resolution is now released. The underlying observation network is composed of four sites over the two typical surface types in the YRD. At each site, meteorological conditions, four radiation components, EC measurements and soil hydrothermal are examined. This dataset is provided in a XLSX format which can be easily accessed and used by the atmosphere, hydrology, ecology and 80 cryosphere communities, aiming to facilitate the coherence and continuity in scientific understanding of the interactions among the multi-sphere coupled systems in the YRD. These data will be valuable for validating remote-sensing data products, evaluating meteorological and air-quality models (Tsai et al., 2007), and improving boundary-layer parameterization schemes (Bian et al., 2002; Zhang et al., 2020).

In the present work, we provide a long-term (2011–2019) half-hourly-resolution dataset of the integrated land–atmosphere interaction observations over the two typical landscapes (i.e., cropland and suburb) in the YRD and make this 85 dataset available to the public. The paper is organized as follows: Section 2 describes the sites, instruments, and data processing methods; Section 3 quantifies the meteorological, solar radiation, heat, and CO₂ fluxes at diurnal and seasonal scales at four sites; the availability of the dataset is introduced in Section 4, and a conclusion is shown in Section 5.

2 Materials and methods

2.1 Sites

90 The integrated land–atmosphere interaction observation data shown in the present work were collected at four experiment sites including two cropland (i.e., Shouxian and Dongtai station) and two suburb areas (Xuzhou and Dongshan station) of the YRD (Figure 1), which are hereinafter referred to as SX-cropland, DT-cropland, XZ-suburb, and DS-suburb, respectively.

The XZ-suburb site (34.22° N, 117.14° E; 44 m above sea level, Figure 1a) is located in the northwest corner of the 95 Nanhu Campus of China University of Mining and Technology in Tongshan New District, Jiangsu Province, China. A road is approximately 100 m north of the flux tower with a huge traffic volume. To the north of the road is a park, which is

dominantly covered by vegetation and lakes. To the south of the observatory are school buildings (mean height 4.5 m), with high population density, low traffic flow, and high vegetation coverage. Easterly and southeasterly winds prevailed at this site (Figure 2).

100 The SX-cropland site (32.44° N, 116.79° E; 27 m above sea level, Figure 1b) is situated at Shouxian Agro-Ecosystem Station in Anhui Province, China. The site is characterized by the flat terrain and is covered with silty clay loam soil. The nearest village is over 500 m far away from the observation site. A rice–wheat rotation system was practiced around the EC flux tower. Over this rice–wheat rotation cropland, winter wheat grows from October to June whereas for summer rice it is from June to September every year (Chen et al., 2015). The dominant wind direction ranged from the southeast in spring to 105 the northwest in winter (Figure 2).

110 The DT-cropland site (32.76° N, 120.47° E; 4 m above sea level, Figure 1d) is about 45 km west of the East China Sea in Jiangsu Province, China. The soil at the site is predominantly clay. The site is homogeneous with a rotation of summer rice and winter wheat cultivated in the field (Li et al., 2017; Duan et al., 2021a). Here, winter wheat grows from December to May while summer rice grows from June to November every year. The dominant wind direction ranged from the southeast in spring to the northwest in winter (Figure 2).

115 The DS-suburb site (31.08° N, 120.43° E; 13 m above sea level, Figure 1e) is on the southeast shore of Lake Taihu in Jiangsu Province, China (Wang et al., 2014). The observation site is surrounded by water, cropland, and rural houses. The prevailing wind in this area is southeast in summer and northeast in winter (Figure 2, Lee et al., 2014).

120 For four sites, aerodynamic roughness length [z_0 , method of Martano (2000)] showed significant seasonal patterns, with the monthly median values of 0.01–0.09 m for SX-cropland, 0.09–0.38 m for DT-cropland, 0.74–1.32 m for XZ-suburb, and 0.44–1.14 m for DS site, respectively (Figure 3).

2.2 Instruments

125 All four sites are equipped with an EC system for long-term, continuous monitoring of the surface radiation, H , λE and CO_2 fluxes. Table 1 shows the details of instruments at all four sites. The EC system consists of a three-dimensional sonic anemometer (IRGASON, Campbell Scientific Incorporation, USA at XZ-suburb site; CSAT3, Campbell Scientific Incorporation, USA at three other sites) and a CO_2/H_2O open-path infrared gas analyzer (EC 150, Campbell Scientific Incorporation, USA at SX-cropland site; LI-7500, LI-COR Biosciences, Inc., USA at DT-cropland and DS-suburb sites; IRGASON, Campbell Scientific Incorporation, USA at XZ-suburb site). The EC measurement height was 2.5 m at SX-cropland, 10 m at DT-cropland, 16.5 m at XZ-suburb, and 20 m above ground level (AGL) at DS-suburb site. The four-component net radiometers (CNR-4, Kipp & Zonen B.V., Delft, the Netherlands) were mounted at 1.5 m for SX-cropland and DS-suburb, 3 m for DT-cropland, and 26.5 m AGL for XZ-suburb sites, respectively. Additionally, the soil heat flux (G , using Hukseflux Thermal Sensors HFP01 heat flux plates) was measured at 0.05 m below the ground surface for the SX-cropland site, 0.05, 0.1, 0.2, and 0.4 m for the DT-cropland site, 0.05 m for XZ-suburb site, and 0.05 and 0.10 m for DS-suburb site. Other measurements including air humidity and air temperature (HMP155A; Vaisala, Inc, Helsinki, Finland at

130 SX-cropland and XZ-suburb sites; HMP 45A; Vaisala, Inc, Helsinki, Finland at DT-cropland site, and HMP45C; Vaisala, Inc, Helsinki, Finland at DS-suburb site) and surface air pressure (PTB110, Vaisala, Inc, Helsinki, Finland) were at a height of 2.5 m at SX-cropland, 10 m at DT-cropland, 16.5 m at XZ-suburb and 20 m at DS-suburb site. All instruments were calibrated by professional engineers. For example, the calibration steps of CO₂/H₂O open-path infrared gas analyzer mainly included: (a) determining the calibration coefficients and (b) setting zero and span. The three-dimensional sonic anemometer
135 needed a factory calibration (i.e., test for wind offset and check for diagnostic flags) every two years, while the four-component net radiometer was calibrated every year to guarantee the radiation data quality. More detailed information about the instruments are available in Lee et al. (2014), Duan et al. (2021a), and Duan et al. (2021b).

2.3 Data processing

Each site was visited biweekly to monthly, to maintain instruments as well as download EC data. To gain the high-
140 quality 30-min-resolution EC data, a series of post-processing steps were performed as follows (see Figure 4):

- (1) The raw 10-Hz EC data, including longitudinal (u), lateral (v), and vertical (w) wind velocities, sonic temperature (T_s), and water vapor (H₂O) density were sampled by a datalogger (model CR3000, Campbell Scientific Inc.) and then transformed into 30 min binaries with the Campbell Scientific LoggerNet 4.2.1 software.
- (2) The LI-COR EddyPro 6.2.1 software was used to calculate and correct 30 min turbulent fluxes of H , λE , and
145 CO₂ fluxes, where the data processing includes: (a) spike removal based on the algorithm of Vickers and Mahrt (1997), i.e., statistical outliers beyond ± 3.5 standard deviation in a running window of 10 values were rejected, except more than three values in a row met this criterion (Schmidt et al., 2012), (b) time delay compensation, (c) double coordinate rotation for the sonic anemometer tilt correction, (d) spectral correction, (e) virtual temperature correction for H (Lee et al., 2004), and (f) Webb–Pearman–Leuning density fluctuations for λE and CO₂ fluxes
150 (Webb et al., 1980).
- (3) The quality control of eddy covariance measurements includes stationarity test, integrated turbulence characteristics test, and footprint analysis. The EddyPro quality flags based on those steps include “high quality” (flag 0), “suitable for budget analysis” (flag 1), and “discard” (flag 2). Note that EC data under unfavorable weather conditions (e.g., rainy and foggy days) or during periods of instrument malfunctions were excluded.
155 However, there was no interpolation in the measurement, which can keep initial information of observations.

In this paper, the footprint model proposed by Kljun et al. (2015) was used to examine the spatial representativeness of the EC fluxes at four sites (Figure 5). The average fetch length of the 90% source area was estimated as 225 m, 800 m, 1035 m, and 1558 m for SX-cropland, DT-cropland, XZ-suburb, and DS-suburb flux tower. Based on the results in Figure 5, the land cover fractions were retrieved from the Google Earth image. The compositions in half-hourly EC 90% probable
160 footprints of the flux tower were separated into five categories: forest, built-up area, cropland, grassland, and water. As shown in Table 2, cropland was the dominant land cover type at SX-cropland and DT-cropland sites, with a fraction of 94% at both sites. From the analysis of the 30-min 90% footprints during the measurement periods, XZ-suburb site consisted of

53 % built-up area, 31 % grassland, 13 % forest, and 3 % water. Whereas for DS-suburb site, the 30-min EC 90 % probable footprint (Kljun et al. 2015) climatology consisted of built-up area and cropland equally (Table 2).

165 Radiative fluxes and meteorological variables were sampled at 1 Hz by the CR3000 datalogger, from which the 30-min means were estimated. The radiative fluxes were limited to physically plausible thresholds, with nocturnal shortwave radiation forced to 0 W m⁻² (Michel et al., 2008). The meteorological data quality control checks involved reasonable range, internal consistency, and temporal and spatial consistency based on the methods in Ren et al. (2015). The coverage rates of meteorological, radiative, heat, and CO₂ fluxes data, together with their proportions of the 30-min high-quality measurements
170 are summarized in Table 3.

2.4 Methods

R_n (positive radiation toward the surface) is derived from incoming (↓, downward) and outgoing (↑, upward) components of shortwave radiation (K) and longwave radiation (L):

$$R_n = K_{\downarrow} + L_{\downarrow} - K_{\uparrow} - L_{\uparrow}. \quad (1)$$

175 H and λE (positive flux away from the surface) are estimated by the EC methods (Kaimal and Finnigan, 1994):

$$H = \rho c_p \overline{w' T'}, \quad (2)$$

$$\lambda E = \lambda \frac{M_w/M_a}{\bar{P}} \bar{\rho} \overline{w' e'}, \quad (3)$$

where w' , T' , and e' are the turbulent fluctuations from the mean of the vertical wind velocity (m s⁻¹), air temperature (K), and water vapor pressure (hPa), respectively, ρ is the air density (kg m⁻³), c_p is the specific heat capacity of air at constant pressure (J kg⁻¹ K⁻¹), λ is the latent heat of vaporization (J kg⁻¹), M_w and M_a are the water and air molar mass (g mol⁻¹), and P is the air pressure (hPa).

180 F_c (positive CO₂ flux away from the surface) is calculated as follows (Ohtaki and Matsui, 1982):

$$F_c = \overline{w' c'}, \quad (4)$$

where c' is the fluctuation in the concentration of CO₂ (μmol m⁻³).

185 3 Results

To advance the knowledge of the land–atmosphere interaction in the YRD, and facilitate the comparison of the similarities and differences between the two typical land surface types, the analysis in 2016 were selected as an example in this section, due to the available measurements at all the four sites.

3.1 Meteorological variables

190 The seasonal (spring, March–May; summer, June–August; autumn, September–November; and winter, December–February) dynamics of air temperature (T) were obvious across all four sites, with an annual mean varied between 16 °C and 17.5 °C (Figure 6a). The average monthly T was relatively high in summer (26–27 °C) but low in winter (4–7 °C) among the four sites. The differences in the T between the four sites were minimal. During the observation period, the annual mean wind speed (WS) was the highest at the DS-suburb site ($\sim 3 \text{ m s}^{-1}$) as it was measured at the highest 195 observation height (at 20 m AGL, Figure 6b). The annual mean relative humidities at the two cropland sites (i.e. 74 % for SX-cropland and 80 % for DT-cropland sites) were larger than those at the two suburb sites (i.e. both 66 % for XZ-suburb and DS-suburb sites, Figure 6c). The seasonal variations in air pressure (P) were opposite to those in air temperature at all four sites (Figures 6a and d). P was high in winter (1023–1025 hPa) but low in summer (1002–1005 hPa) across all the four sites (Figure 6d).

200 3.2 Surface radiation budget

At four sites, four surface radiative fluxes [incoming shortwave radiation (K_{\downarrow}), outgoing shortwave radiation (K_{\uparrow}), 205 incoming longwave radiation (L_{\downarrow}), outgoing longwave radiation (L_{\uparrow})] and the surface albedo varied seasonally (Figure 7) and diurnally (Figure 8) with the solar altitude (You et al., 2017). In addition, the seasonal variations in K_{\downarrow} received at the surface were also greatly affected by weather and cloud conditions (Chen et al., 2016b; Duan et al., 2021a). For instance, the 210 highest daily mean K_{\downarrow} was 317 W m⁻² for SX-cropland, 329 W m⁻² for DT-cropland, 336 W m⁻² for DS-suburb sites in May 2016, and 332 W m⁻² for XZ-suburb site in June 2016, respectively (Figure 7a). From May to June, the weather is sunny with fewer clouds resulting in the higher daily mean K_{\downarrow} despite the lower solar altitudes. The daily mean peak values of K_{\downarrow} were 215 67 W m⁻² for SX-cropland, 51 W m⁻² for DT-cropland, 50 W m⁻² for XZ-suburb sites, and 73 W m⁻² for DS-suburb sites, respectively (Figure 7b). The phenomenon from Guo et al. (2016) that K_{\downarrow} varied with both K_{\downarrow} and surface albedo was also similar with our present findings. For example, the highest daily mean K_{\downarrow} at the SX-cropland site that occurred on 29 November 2016 was mainly due to the high snow albedo (Figure 7e). On the other hand, L_{\downarrow} largely relied on air temperature, 220 cloud properties, and water vapor (Flerchinger et al., 2009), which explains the daily mean L_{\downarrow} smallest in cold winter but largest in warm and wet summer with the peak daily means of 484, 459, 458, and 450 W m⁻² for SX-cropland, DT-cropland, XZ-suburb, and DS-suburb sites, respectively (Figure 7c). L_{\downarrow} is closely related to the surface temperature and emissivity (Chen et al., 2016b), consist with the daily mean L_{\downarrow} with the maximum values in summer, i.e., 521 W m⁻² for SX-cropland, 225 501 W m⁻² for DT-cropland, 501 W m⁻² for XZ-suburb, and 516 W m⁻² for DS-suburb sites, respectively (Figure 7d).

The diurnal cycles of the four radiation components for different months are shown in Figure 8. As expected, K_{\downarrow} exhibits the strongest amplitude of the diurnal cycle among all the four radiation components, reaching up to 675 W m⁻² for SX-cropland, 747 W m⁻² for DT-Cropland, 691 W m⁻² for XZ-suburb, and 847 W m⁻² for DS-suburb sites, respectively

220 K_{\uparrow} shows the similar diurnal variation trends with K_{\downarrow} . The monthly mean diurnal maxima of K_{\uparrow} were 104 W m⁻² for SX-cropland, 101 W m⁻² for DT-cropland, 86 W m⁻² for XZ-suburb, and 178 W m⁻² for DS-suburb sites, respectively (Figure 8b). Both L_{\downarrow} and L_{\uparrow} present a smaller diurnal cycle amplitude, with slightly higher values in the afternoon [around 14:00–15:00 Local Time (LT)]. Surface albedo ($K_{\uparrow}/K_{\downarrow}$) directly modulates the energy absorbed by the surface, which is mainly influenced by surface conditions, solar angle, and weather conditions (Zhang et al., 2014). The 225 midday (10:00–15:00 LT) albedo varied diurnally between 0.1 and 0.26. The annual mean albedo was 0.163, 0.133, 0.143, and 0.195 for SX-cropland, DT-Cropland, XZ-suburb, and DS-suburb sites, respectively (Figure 8e).

3.3 Surface energy fluxes

The surface energy balance fluxes play a key role in regulating the ground thermal regime (Hoelzle et al., 2022). Figure 230 9 shows the remarkable seasonal variations in daily mean R_n , λE , H , and G at a depth of 0.05 m ($G_{0.05}$). Both R_n and $G_{0.05}$ were high in spring and summer but low in autumn and winter at four sites in the YRD (Figures 9a and 9d). Although in the 235 same climate monsoon area, there existed large differences in λE and H over different surface types. Seasonal variations in λE at two cropland sites had doublet peaks, which were closely related to the crop phenology and agricultural activities (Duan et al., 2021a). For example, daily mean λE firstly increased from 3 W m⁻² (5 W m⁻²) in January to the peak value of 240 110 W m⁻² (182 W m⁻²) in April and then gradually decreased when wheat harvest at the SX-cropland site (DT-cropland site). In mid-June, the rice seedlings were transplanted and daily mean λE attained the second peak of 155 W m⁻² (224 W m⁻²) in August at the SX-cropland site (DT-cropland site). The extensively irrigated cropland enhanced the available energy to support evaporation and resulted in lower H (Dou et al., 2019). Thus, at two cropland sites, the daily mean H was almost lower than 35 W m⁻². However, λE had a unimodal distribution at the DS-suburb site in 2016, with the daily mean peaks of 165 W m⁻² in July (Figure 9b). The daily mean H at XZ-suburb and DS-suburb varied from -21 to 70 W m⁻² and -39 to 81 W m⁻², respectively.

Figure 10 shows the significant diurnal dynamics of R_n , λE , H , and $G_{0.05}$ in all months. As expected, R_n peaked at ~13:00 LT during the daytime due to the strong heating of the surface by the sun, while it was negative ($L_{\uparrow} > L_{\downarrow}$, with $K_{\uparrow} = K_{\downarrow} = 0$, Figure 8) at night when surface radiative cooling dominated (Nelli et al., 2020). The diurnal dynamics of R_n varied 245 from -38 to 528, -38 to 590, -61 to 513, and -64 to 562 W m⁻² for SX-cropland, DT-cropland, XZ-suburb, and DS-suburb sites, respectively. At the two cropland sites, λE was the largest consumer of the R_n in the whole year with the annual mean midday $\lambda E/R_n$ of 35 % and 58 % at SX-cropland and DT-cropland sites. At the two suburb sites, the midday H/R_n ranged between 4 % and 55 % (16 % and 70 %) for the XZ-suburb site (the DS-suburb site), while $\lambda E/R_n$ ranged between 4 % and 250 49 % (29 % and 93 %) for the XZ-suburb site (DS-suburb site), and the largest consumer of R_n shifted between λE and H . These seasonal fluctuations in λE and H at the two suburb areas were mainly due to the seasonal cycles of the vegetation cover and the intensive human activities (Duan et al., 2021a). The $G_{0.05}$ was small and varied between -20 and 40 W m⁻²

diurnally. Generally, radiation and heat fluxes showed distinct differences under the typical surface types in the monsoon area of the YRD, China.

3.4 Carbon flux

Figure 11a exhibits the seasonal variations of the daily mean CO_2 flux. At the two rice-wheat rotation cropland sites, the CO_2 flux measured the photosynthesis and respiration of the crops. At the beginning of the rice growing period (June) the CO_2 emission was high at the two cropland sites, with the peak daily mean CO_2 flux value of $2.4 \text{ } \mu\text{mol m}^{-2} \text{ s}^{-1}$ for SX-cropland and $5.5 \text{ } \mu\text{mol m}^{-2} \text{ s}^{-1}$ for DT-cropland site, respectively. This was mainly caused by the CO_2 released from aquatic weeds and algae on the paddy water surface (Nishimura et al., 2015). The daily mean CO_2 flux reached its minima in August (– $11 \text{ } \mu\text{mol m}^{-2} \text{ s}^{-1}$ for SX-cropland and – $10 \text{ } \mu\text{mol m}^{-2} \text{ s}^{-1}$ for DT-cropland site) when the rice photosynthetic rates were quite strong. Afterwards, the rice leaves gradually turned yellow and tended to mature. The wheat field had similar patterns to the rice paddy. At the XZ-suburb site, the daily mean CO_2 flux was almost positive in spring, autumn and winter, and the maximum daily mean value reached $6.5 \text{ } \mu\text{mol m}^{-2} \text{ s}^{-1}$, indicating the domination of human activities (e.g., greater residential heating). At the DS-suburb site, the daily mean CO_2 flux varied between – 4 and $3 \text{ } \mu\text{mol m}^{-2} \text{ s}^{-1}$, with high values in May and low values in September.

A marked and significant diurnal cycle of CO_2 flux is shown in Figure 11b. Positive nocturnal values, respectively reaching at $6.4, 8.2, 8.2, 4.5 \text{ } \mu\text{mol m}^{-2} \text{ s}^{-1}$ for SX-cropland, DT-cropland, XZ-suburb, and DS-suburb sites, were mainly related to the poor night-time atmospheric mixing (Cheng et al., 2018), lower boundary layer height (Hassan, 2015), plant respiration (Mai et al., 2020), and anthropogenic sources (Hu et al., 2018). The mid-afternoon negative CO_2 fluxes (about – $8\text{--}29 \text{ } \mu\text{mol m}^{-2} \text{ s}^{-1}$, negative values refer that the ecosystem absorbs CO_2 from the atmosphere) at SX-cropland, DT-cropland, XZ-suburb, and DS-suburb sites were due to the active biospheric photosynthesis and favorable dispersion conditions (Grimmond et al., 2002). However, the CO_2 flux almost remained positive in January and December; i.e., suburb surface was a net CO_2 source. The vegetation in XZ-suburb had a clear effect during the daytime, but it was not enough to offset the strong anthropogenic emissions, which are significant during rush hours in the morning and afternoon (Figure 11b).

275 4 Data availability

All datasets presented in this paper are freely available at <https://doi.org/10.5281/zenodo.6552301>, last access: 10 May 2022 (Duan et al., 2022). The local time (UTC+8) was used at four sites.

5 Conclusion

The turbulent flux parameters in current numerical models suffer from poor representation in the monsoon region, especially in the YRD, as it is experiencing rapid land-use changes. Thus, continuous (2011–2019) and high-quality land-

atmosphere interaction observations are needed to be collected for understanding of the land surface processes in the YRD. In this paper, field measurements over two typical underlying surfaces, i.e., cropland and suburb surface, were presented at four different sites in the monsoonal YRD region. Our findings showed that the individual radiation components, H , λE , G , and CO_2 fluxes exhibited diurnal and seasonal variations, which also depended on the local underlying surface conditions.

285 Take the Year of 2016 as an example, λE dominated the land–atmosphere heat flux exchange at two cropland sites (SX-cropland and DT-cropland). However, the dominant consumer of the R_n fluctuated between λE and H at two suburb sites (XZ-suburb and DS-suburb), which could subsequently modulate the local climate.

Generally, this dataset provides comprehensive, high-temporal-resolution and high-quality in situ flux observations in the YRD, which has the potentials for studying land–atmosphere interactions and their impacts on weather change research.

290 In addition, this dataset could provide accurate parameters and calibrations for reanalysis data, remote sensing products, and climate models.

Author contributions

GZ, QK, and YY designed the experiments and carried them out. DZ, XQ, and ZS performed data processing, organization, and figure generation. DZ and YY wrote the manuscript, and all authors participated in the revision of the paper.

295 Competing interests

The authors declare that they have no conflict of interest.

Acknowledgments

We sincerely thank all the scientists, engineers, and students who participated in the field campaigns, maintained the measurement instruments, and processed the observations. We thank the anonymous reviewers for their useful comments
300 and suggestions. We thank the Level-1 and Atmosphere Archive & Distribution System Distributed Active Archive Center for the MODIS MCD12Q1 data (source: <https://ladsweb.modaps.eosdis.nasa.gov/search/>, last access: 17 August 2022).

Financial support

This work was funded by the National Natural Science Foundation of China (Grant: 41875013), and the Postgraduate Research & Practice Innovation Program of Jiangsu Province (KYCX21_0950).

Ao, X., Grimmond, C. S. B., Chang, Y., Liu, D., Tang, Y., Hu, P., Wang, Y., Zou, J., and Tan, J.: Heat, water and carbon exchanges in the tall megacity of Shanghai: challenges and results, *International Journal of Climatology*, 36, 4608–4624, <https://doi.org/10.1002/joc.4657>, 2016.

Baldocchi, D. and Ma, S.: How will land use affect air temperature in the surface boundary layer? Lessons learned from a 310 comparative study on the energy balance of an oak savanna and annual grassland in California, USA, *Tellus Series B-Chemical and Physical Meteorology*, 65, <https://doi.org/10.3402/tellusb.v65i0.19994>, 2013.

Baldocchi, D. D.: Assessing the eddy covariance technique for evaluating carbon dioxide exchange rates of ecosystems: past, 315 present and future, *Global Change Biology*, 9, 479–492, <https://doi.org/10.1046/j.1365-2486.2003.00629.x>, 2003.

Bi, X., Gao, Z., Deng, X., Wu, D., Liang, J., Zhang, H., Sparrow, M., Du, J., Li, F., and Tan, H.: Seasonal and diurnal 320 variations in moisture, heat, and CO₂ fluxes over grassland in the tropical monsoon region of southern China, *Journal of Geophysical Research: Atmospheres*, 112, <https://doi.org/10.1029/2006JD007889>, 2007.

Bian, L., Gao, Z., Xu, Q., Lu, L., and Cheng, Y.: Measurements of turbulence transfer in the near-surface layer over the southeastern Tibetan Plateau, *Boundary-layer meteorology*, 102, 281–300, <https://doi.org/10.1023/A:1013177629245>, 2002.

320 Chen, C., Li, D., Gao, Z., Tang, J., Guo, X., Wang, L., and Wan, B.: Seasonal and Interannual Variations of Carbon Exchange over a Rice-Wheat Rotation System on the North China Plain, *Advances in Atmospheric Sciences*, 32, 1365–1380, <https://doi.org/10.1007/s00376-015-4253-1>, 2015.

Chen, H., Zhang, Y., Yu, M., Hua, W., Sun, S., Li, X., and Gao, C.: Large-scale urbanization effects on eastern Asian 325 summer monsoon circulation and climate, *Climate Dynamics*, 47, 117–136, <https://doi.org/10.1007/s00382-015-2827-3>, 2016a.

Chen, H. S. and Zhang, Y.: Sensitivity experiments of impacts of large-scale urbanization in East China on East Asian winter monsoon, *Chinese Science Bulletin*, 58, 809–815, <https://doi.org/10.1007/s11434-012-5579-z>, 2013.

Chen, S., Yang, Y., Deng, F., Zhang, Y., Liu, D., Liu, C., and Gao, Z.: A high-resolution monitoring approach of canopy 330 urban heat island using a random forest model and multi-platform observations, *Atmos. Meas. Tech.*, 15, 735–756, <https://doi.org/10.5194/amt-15-735-2022>, 2022.

Chen, X., Yu, Y., Chen, J., Zhang, T., and Li, Z.: Seasonal and interannual variation of radiation and energy fluxes over a rain-fed cropland in the semi-arid area of Loess Plateau, northwestern China, *Atmospheric Research*, 176–177, 240–253, <https://doi.org/10.1016/j.atmosres.2016.03.003>, 2016b.

Cheng, X. L., Liu, X. M., Liu, Y. J., and Hu, F.: Characteristics of CO₂ Concentration and Flux in the Beijing Urban Area, 335 *Journal of Geophysical Research: Atmospheres*, 123, 1785–1801, <https://doi.org/10.1002/2017JD027409>, 2018.

Cuntz, M., Mai, J., Samaniego, L., Clark, M., Wulfmeyer, V., Branch, O., Attinger, S., and Thober, S.: The impact of standard and hard-coded parameters on the hydrologic fluxes in the Noah-MP land surface model, *Journal of Geophysical Research: Atmospheres*, 121, 10,676–610,700, <https://doi.org/10.1002/2016JD025097>, 2016.

Dai, S., Ju, W., Zhang, Y., He, Q., Song, L., and Li, J.: Variations and drivers of methane fluxes from a rice-wheat rotation agroecosystem in eastern China at seasonal and diurnal scales, *Science of The Total Environment*, 690, 973–990, <https://doi.org/10.1016/j.scitotenv.2019.07.012>, 2019.

Dou, J., Grimmond, S., Cheng, Z., Miao, S., Feng, D., and Liao, M.: Summertime surface energy balance fluxes at two Beijing sites, *International Journal of Climatology*, 39, 2793–2810, <https://doi.org/10.1002/joc.5989>, 2019.

Duan, Z., Gao, Z., Xu, Q., Zhou, S., Qin, K., and Yang, Y.: A benchmark dataset of diurnal- and seasonal-scale radiation, heat and CO₂ fluxes in a typical East Asian monsoon region [Dataset], in, Zenodo, <https://doi.org/10.5281/zenodo.6552301>, 2022.

Duan, Z., Grimmond, C. S. B., Gao, C. Y., Sun, T., Liu, C., Wang, L., Li, Y., and Gao, Z.: Seasonal and Interannual Variations in the Surface Energy Fluxes of a Rice–Wheat Rotation in Eastern China, *Journal of Applied Meteorology and Climatology*, 60, 877–891, <https://doi.org/10.1175/jamc-d-20-0233.1>, 2021a.

Duan, Z., Yang, Y., Wang, L., Liu, C., Fan, S., Chen, C., Tong, Y., Lin, X., and Gao, Z.: Temporal characteristics of carbon dioxide and ozone over a rural-cropland area in the Yangtze River Delta of eastern China, *Science of The Total Environment*, 757, 143750, <https://doi.org/10.1016/j.scitotenv.2020.143750>, 2021b.

Feddema, J. J., Oleson, K. W., Bonan, G. B., Mearns, L. O., Buja, L. E., Meehl, G. A., and Washington, W. M.: The importance of land-cover change in simulating future climates, *Science (New York, N.Y.)*, 310, 1674–1678, <https://doi.org/10.1126/science.1118160>, 2005.

Flerchinger, G. N., Xaio, W., Marks, D., Sauer, T. J., and Yu, Q.: Comparison of algorithms for incoming atmospheric long-wave radiation, *Water Resources Research*, 45, <https://doi.org/10.1029/2008WR007394>, 2009.

Gao, Z., Chae, N., Kim, J., Hong, J., Choi, T., and Lee, H.: Modeling of surface energy partitioning, surface temperature, and soil wetness in the Tibetan prairie using the Simple Biosphere Model 2 (SiB2), *Journal of Geophysical Research: Atmospheres*, 109, <https://doi.org/10.1029/2003JD004089>, 2004.

Ge, H., Zhang, H., Zhang, H., Cai, X., Song, Y., and Kang, L.: The characteristics of methane flux from an irrigated rice farm in East China measured using the eddy covariance method, *Agricultural and Forest Meteorology*, 249, 228–238, <https://doi.org/10.1016/j.agrformet.2017.11.010>, 2018.

Grimmond, C. S. B., King, T. S., Cropley, F. D., Nowak, D. J., and Souch, C.: Local-scale fluxes of carbon dioxide in urban environments: methodological challenges and results from Chicago, *Environmental Pollution*, 116, S243–S254, [https://doi.org/10.1016/S0269-7491\(01\)00256-1](https://doi.org/10.1016/S0269-7491(01)00256-1), 2002.

Guo, W., Wang, X., Sun, J., Ding, A., and Zou, J.: Comparison of land–atmosphere interaction at different surface types in the mid- to lower reaches of the Yangtze River valley, *Atmos. Chem. Phys.*, 16, 9875–9890, <https://doi.org/10.5194/acp-16-9875-2016>, 2016.

370 Hassan, A. A.: Diurnal and Monthly Variations in Atmospheric CO₂ Level in Qena, Upper Egypt, *Resources and Environment*, 5, 59–65, <https://doi.org/10.5923/j.re.20150502.02>, 2015.

Hoelzle, M., Hauck, C., Mathys, T., Noetzli, J., Pellet, C., and Scherler, M.: Long-term energy balance measurements at three different mountain permafrost sites in the Swiss Alps, *Earth Syst. Sci. Data*, 14, 1531–1547, <https://doi.org/10.5194/essd-14-1531-2022>, 2022.

375 Hu, C., Liu, S. D., Wang, Y. W., Zhang, M., Xiao, W., Wang, W., and Xu, J. P.: Anthropogenic CO₂ emissions from a megacity in the Yangtze River Delta of China, *Environmental Science and Pollution Research*, 25, 23157–23169, <https://doi.org/10.1007/s11356-018-2325-3>, 2018.

Huang, W., Griffis, T. J., Hu, C., Xiao, W., and Lee, X.: Seasonal Variations of CH₄ Emissions in the Yangtze River Delta Region of China Are Driven by Agricultural Activities, *Advances in Atmospheric Sciences*, 38, 1537–1551, 380 <https://doi.org/10.1007/s00376-021-0383-9>, 2021.

Jin, Y. and Roy, D. P.: Fire-induced albedo change and its radiative forcing at the surface in northern Australia, *Geophysical Research Letters*, 32, <https://doi.org/10.1029/2005GL022822>, 2005.

Kaimal, J. C. and Finnigan, J. J.: *Atmospheric Boundary Layer Flows: Their Structure and Measurement*, Oxford University Press, New York, 302 pp., <https://doi.org/10.1093/oso/9780195062397.001.0001>, 1994.

385 Kang, M. and Cho, S.: Progress in water and energy flux studies in Asia: A review focused on eddy covariance measurements, *Journal of Agricultural Meteorology*, 77, 2–23, <https://doi.org/10.2480/agrmet.D-20-00036>, 2021.

Kljun, N., Calanca, P., Rotach, M. W., and Schmid, H. P.: A simple two-dimensional parameterisation for Flux Footprint Prediction (FFP), *Geoscientific Model Development*, 8, 3695–3713, <https://doi.org/10.5194/gmd-8-3695-2015>, 2015.

390 Lee, B., Kim, N., Kim, E., Jang, K., Kang, M., Lim, J., Cho, J., and Lee, Y.: An Artificial Intelligence Approach to Predict Gross Primary Productivity in the Forests of South Korea Using Satellite Remote Sensing Data, *Forests*, 11, 1000, <https://doi.org/10.3390/f11091000>, 2020.

Lee, X., Massman, W., and Law, B.: *Handbook of micrometeorology : a guide for surface flux measurement and analysis*, in, Springer Science & Business Media, 2004.

395 Lee, X., Liu, S., Xiao, W., Wang, W., Gao, Z., Cao, C., Hu, C., Hu, Z., Shen, S., Wang, Y., Wen, X., Xiao, Q., Xu, J., Yang, J., and Zhang, M.: The Taihu Eddy Flux Network: An Observational Program on Energy, Water, and Greenhouse Gas Fluxes of a Large Freshwater Lake, *Bulletin of the American Meteorological Society*, 95, 1583–1594, <https://doi.org/10.1175/BAMS-D-13-00136.1>, 2014.

Li, D. and Wang, L.: Sensitivity of Surface Temperature to Land Use and Land Cover Change-Induced Biophysical Changes: The Scale Issue, *Geophysical Research Letters*, 46, 9678–9689, <https://doi.org/10.1029/2019GL084861>, 2019.

400 Li, D., Sun, T., Liu, M. F., Yang, L., Wang, L. L., and Gao, Z. Q.: Contrasting responses of urban and rural surface energy budgets to heat waves explain synergies between urban heat islands and heat waves, *Environmental Research Letters*, 10, <https://doi.org/10.1088/1748-9326/10/5/054009>, 2015.

Li, Q. and Xue, Y. K.: Simulated impacts of land cover change on summer climate in the Tibetan Plateau, *Environmental Research Letters*, 5, <https://doi.org/10.1088/1748-9326/5/1/015102>, 2010.

405 Li, X., Gao, Z., Li, Y., and Tong, B.: Comparison of Sensible Heat Fluxes Measured by a Large Aperture Scintillometer and Eddy Covariance System over a Heterogeneous Farmland in East China, *Atmosphere*, 8, <https://doi.org/10.3390/atmos8060101>, 2017.

Mai, B., Deng, X., Zhang, F., He, H., Luan, T., Li, F., and Liu, X.: Background Characteristics of Atmospheric CO₂ and the 410 Potential Source Regions in the Pearl River Delta Region of China, *Advances in Atmospheric Sciences*, 37, 557–568, <https://doi.org/10.1007/s00376-020-9238-z>, 2020.

Martano, P.: Estimation of Surface Roughness Length and Displacement Height from Single-Level Sonic Anemometer Data, *Journal of Applied Meteorology*, 39, 708–715, [https://doi.org/10.1175/1520-0450\(2000\)039<0708:eosrla>2.0.co;2](https://doi.org/10.1175/1520-0450(2000)039<0708:eosrla>2.0.co;2), 2000.

415 Michel, D., Philipona, R., Ruckstuhl, C., Vogt, R., and Vuilleumier, L.: Performance and Uncertainty of CNR1 Net Radiometers during a One-Year Field Comparison, *Journal of Atmospheric and Oceanic Technology*, 25, 442–451, <https://doi.org/10.1175/2007JTECHA973.1>, 2008.

Nelli, N. R., Temimi, M., Fonseca, R. M., Weston, M. J., Thota, M. S., Valappil, V. K., Branch, O., Wizemann, H.-D., 420 Wulfmeyer, V., and Wehbe, Y.: Micrometeorological measurements in an arid environment: Diurnal characteristics and surface energy balance closure, *Atmospheric Research*, 234, 104745, <https://doi.org/10.1016/j.atmosres.2019.104745>, 2020.

Nishimura, S., Yonemura, S., Minamikawa, K., and Yagi, K.: Seasonal and diurnal variations in net carbon dioxide flux throughout the year from soil in paddy field, *Journal of Geophysical Research: Biogeosciences*, 120, 63–76, <https://doi.org/10.1002/2014JG002746>, 2015.

425 Ohtaki, E. and Matsui, T.: Infrared device for simultaneous measurement of fluctuations of atmospheric carbon dioxide and water vapor, *Boundary-Layer Meteorology*, 24, 109–119, <https://doi.org/10.1007/BF00121803>, 1982.

Rao, K. G. and Reddy, N. N.: On Moisture Flux of the Indian Summer Monsoon: A New Perspective, *Geophysical Research Letters*, 46, 1794–1804, <https://doi.org/10.1029/2018GL080392>, 2019.

Ren, Z., Zhang, Z., Sun, c., Liu, Y., Li, J., Ju, X., Zhao, Y., Li, Z., Zhang, W., Li, H., Zeng, X., Re, X., Liu, Y., and Wang, 430 H.: Development of three-step quality control system of real-time observation data from AWS in China (in Chinese), *Meteorol. Monthly*, 41, 1268–1277, <https://doi.org/10.7519/j.issn.1000-0526.2015.10.010>, 2015.

Schmidt, M., Reichenau, T. G., Fiener, P., and Schneider, K.: The carbon budget of a winter wheat field: An eddy covariance analysis of seasonal and inter-annual variability, *Agricultural and Forest Meteorology*, 165, 114–126, <https://doi.org/10.1016/j.agrformet.2012.05.012>, 2012.

435 Sun, T., Wang, Z. H., and Ni, G. H.: Revisiting the hysteresis effect in surface energy budgets, *Geophysical Research Letters*, 40, 1741–1747, <https://doi.org/10.1002/grl.50385>, 2013.

440 Tsai, J., Tsuang, B., Lu, P., Yao, M., and Shen, Y.: Surface Energy Components and Land Characteristics of a Rice Paddy, Journal of Applied Meteorology and Climatology, 46, 1879–1900, <https://doi.org/10.1175/2007jamc1568.1>, 2007.

Vickers, D. and Mahrt, L.: Quality Control and Flux Sampling Problems for Tower and Aircraft Data, Journal of Atmospheric and Oceanic Technology, 14, 512–526, [https://doi.org/10.1175/1520-0426\(1997\)014<0512:qcrafsp>2.0.co;2](https://doi.org/10.1175/1520-0426(1997)014<0512:qcrafsp>2.0.co;2), 1997.

445 Wang, L., Fan, S., Hu, F., Miao, S., Yang, A., Li, Y., Liu, J., Liu, C., Chen, S., Ho, H. C., Duan, Z., Gao, Z., and Yang, Y.: Vertical Gradient Variations in Radiation Budget and Heat Fluxes in the Urban Boundary Layer: A Comparison Study Between Polluted and Clean Air Episodes in Beijing During Winter, Journal of Geophysical Research: Atmospheres, 125, e2020JD032478, <https://doi.org/10.1029/2020JD032478>, 2020.

450 Wang, W., Xiao, W., Cao, C., Gao, Z., Hu, Z., Liu, S., Shen, S., Wang, L., Xiao, Q., Xu, J., Yang, D., and Lee, X.: Temporal and spatial variations in radiation and energy balance across a large freshwater lake in China, Journal of Hydrology, 511, 811–824, <https://doi.org/10.1016/j.jhydrol.2014.02.012>, 2014.

Webb, E. K., Pearman, G. I., and Leuning, R.: Correction of flux measurements for density effects due to heat and water vapour transfer, Quarterly Journal of the Royal Meteorological Society, 106, 85–100, <https://doi.org/10.1002/qj.49710644707>, 1980.

455 Wei, C., Wang, M., Fu, Q., Dai, C., Huang, R., and Bao, Q.: Temporal characteristics of greenhouse gases (CO₂ and CH₄) in the megacity Shanghai, China: Association with air pollutants and meteorological conditions, Atmospheric Research, 235, 104759, <https://doi.org/10.1016/j.atmosres.2019.104759>, 2020.

460 Xue, Y., Juang, H. M. H., Li, W. P., Prince, S., DeFries, R., Jiao, Y., and Vasic, R.: Role of land surface processes in monsoon development: East Asia and West Africa, Journal of Geophysical Research: Atmospheres, 109, <https://doi.org/10.1029/2003JD003556>, 2004.

Yang, J. and Wang, Z.: Physical parameterization and sensitivity of urban hydrological models: Application to green roof systems, Building and Environment, 75, 250–263, <https://doi.org/10.1016/j.buildenv.2014.02.006>, 2014.

465 Yang, J., Wang, Z., and Huang, H.: Intercomparison of the Surface Energy Partitioning in CMIP5 Simulations, Atmosphere, 10, 602, <https://doi.org/10.3390/atmos10100602>, 2019.

Yang, Y., Zhang, M., Li, Q., Chen, B., Gao, Z., Ning, G., Liu, C., Li, Y., and Luo, M.: Modulations of surface thermal environment and agricultural activity on intraseasonal variations of summer diurnal temperature range in the Yangtze River Delta of China, Science of The Total Environment, 736, 139445, <https://doi.org/10.1016/j.scitotenv.2020.139445>, 2020a.

470 Yang, Y., Fan, S., Wang, L., Gao, Z., Zhang, Y., Zou, H., Miao, S., Li, Y., Huang, M., Yim, S. H. L., and Lolli, S.: Diurnal Evolution of the Wintertime Boundary Layer in Urban Beijing, China: Insights from Doppler Lidar and a 325-m Meteorological Tower, Remote Sensing, 12, 3935, <https://doi.org/10.3390/rs12233935>, 2020b.

470 You, Q., Xue, X., Peng, F., Dong, S., and Gao, Y.: Surface water and heat exchange comparison between alpine meadow
and bare land in a permafrost region of the Tibetan Plateau, *Agricultural and Forest Meteorology*, 232, 48–65,
<https://doi.org/10.1016/j.agrformet.2016.08.004>, 2017.

475 Zhang, Y., Ning, G., Chen, S., and Yang, Y.: Impact of Rapid Urban Sprawl on the Local Meteorological Observational
Environment Based on Remote Sensing Images and GIS Technology, *Remote Sensing*, 13, 2624,
<https://doi.org/10.3390/rs13132624>, 2021.

480 475 Zhang, Y., Wang, X., Hu, R., Pan, Y., and Zhang, H.: Variation of albedo to soil moisture for sand dunes and biological soil
crusts in arid desert ecosystems, *Environmental Earth Sciences*, 71, 1281–1288, <https://doi.org/10.1007/s12665-013-2532-7>, 2014.

485 Zhang, Z., Zhang, M., Cao, C., Wang, W., Xiao, W., Xie, C., Chu, H., Wang, J., Zhao, J., Jia, L., Liu, Q., Huang, W., Zhang,
W., Lu, Y., Xie, Y., Wang, Y., Pu, Y., Hu, Y., Chen, Z., Qin, Z., and Lee, X.: A dataset of microclimate and
radiation and energy fluxes from the Lake Taihu eddy flux network, *Earth Syst. Sci. Data*, 12, 2635–2645,
<https://doi.org/10.5194/essd-12-2635-2020>, 2020.

485

490

495

500

505

510

Table 1. Descriptions of the sensors used at four stations.

Instrument	Site name	Variable (unit)	Model and manufacturer	Installation height (m)	Measurement range	Accuracy
	SX-cropland		CSAT3, Campbell	2.5	u and v : -65 to 65 $m s^{-1}$ w : -65 to 65 $m s^{-1}$	u and v : $\pm 0.04 m s^{-1}$
	DT-cropland		CSAT3, Campbell	10	s^{-1} T_s : -50 °C to 60 °C	w : $\pm 0.02 mm s^{-1}$ T_s : $\pm 0.025 °C$
Three-dimensional sonic anemometer	XZ-suburb	three-dimensional wind speed (u_x , u_y and u_z $m s^{-1}$), sonic air temperature (T_s , °C)	IRGASON, Campbell	16.5	u and v : -65 to 65 $m s^{-1}$ w : -65 to 65 $m s^{-1}$	u and v : $\pm 0.08 m s^{-1}$ w : $\pm 0.04 mm s^{-1}$
					T_s : -50 °C to 60 °C	T_s : $\pm 0.025 °C$
	DS-suburb		CSAT3, Campbell	20	u and v : -65 to 65 $m s^{-1}$ w : -65 to 65 $m s^{-1}$	u and v : $\pm 0.04 m s^{-1}$ w : $\pm 0.02 mm s^{-1}$
	SX-cropland		EC150, Campbell	2.5	CO_2 : 0 to 1830 $mg m^{-3}$ H_2O : 0 to 44 $g m^{-3}$	CO_2 : < 1% H_2O : < 2%
CO ₂ /H ₂ O open-path infrared gas analyzer	DT-cropland	CO ₂ ($mg m^{-3}$), H ₂ O ($mg m^{-3}$)	LI-7500, LI-COR	10	CO ₂ : 0 to 5148 $mg m^{-3}$ H_2O : 0 to 42 $g m^{-3}$	CO ₂ : $\pm 0.2 mg m^{-3}$ H_2O : $\pm 0.02 g m^{-3}$
	XZ-suburb		IRGASON, Campbell	16.5	CO ₂ : 0 to 1830 $mg m^{-3}$ H_2O : 0 to 44 $g m^{-3}$	CO ₂ : $0.2 mg m^{-3}$ H_2O : $0.0035 g m^{-3}$

				CO ₂ : 0 to 5148 mg m ⁻³	
DS-suburb	LI-7500A, LI-COR	20		CO ₂ : ± 0.2 mg m ⁻³	
				H ₂ O: 0 to 42 g m ⁻³	H ₂ O: ± 0.02 g m ⁻³
	SX-cropland	CNR4, Kipp & Zonen	1.5		
Four-component net radiometer	DT-cropland	Radiations (W m ⁻²)	CNR4, Kipp & Zonen	K_{\downarrow} and K_{\uparrow} : 0.3 to 2.8 μ m	K_{\downarrow} and K_{\uparrow} : 5 to 20 μ V W ⁻¹ m ⁻²
	XZ-suburb		CNR4, Kipp & Zonen	L_{\downarrow} and L_{\uparrow} : 4.5 to 42 μ m	L_{\downarrow} and L_{\uparrow} : 5 to 15 μ V W ⁻¹ m ⁻²
	DS-suburb		CNR4, Kipp & Zonen		
Soil heat flux plate	SX-cropland	Soil heat flux (W m ⁻²)	HFP01, Hukseflux	-0.05	
	DT-cropland		HFP01, Hukseflux	-0.05, -0.1, 0.2, and -0.4	± 2000 W m ⁻²
	XZ-suburb		HFP01, Hukseflux	-0.05	
	DS-suburb		HFP01, Hukseflux	-0.05 and -0.10	
Surface atmospheric pressure sensor	SX-cropland	Pressure (P, hPa)	PTB110, Vaisala	2.5	
	DT-cropland		PTB110, Vaisala	10	P: 500 to 1100 hPa
	XZ-suburb		PTB110, Vaisala	16.5	± 0.3 hPa (20 °C)
	DS-suburb		PTB110, Vaisala	20	
Air temperature and humidity	SX-cropland	Air temperature (T_a , °C) and humidity (RH, %)	HMP155A, Vaisala	2.5	T_a : -80 to +60 °C Depends on T_a RH: 0.8 to 100 %
	DT-cropland				T_a : ± 0.2 °C (20 °C) RH: $\pm 2\%$ (0–90%) $\pm 3\%$ (90–100%)
	XZ-suburb				

			<i>RH:</i>	0.8	to	
				100 %		
						<i>T_a:</i> ± 0.2 °C
						(20 °C)
DS-suburb	HMP45C, Vaisala	20	<i>T_a:</i>	-40	to	<i>RH:</i> $\pm 2\%$ (0-
				+60 °C		90%)
						<i>RH:</i> 0 to 100 %
						$\pm 3\%$ (90–100%)

515

520

525

530

535

Table 2. Land cover fractions within the 90 % footprints at four sites.

Site ID		SX-cropland	DT-cropland	XZ-suburb	DS-suburb
Land cover fraction within the 90 % source area	Forest	0.00	0.00	0.13	0.00
	Built-up area	0.04	0.06	0.53	0.50
	Cropland	0.94	0.94	0.00	0.50
	Grassland	0.00	0.00	0.31	0.00
	Water	0.02	0.00	0.03	0.00

540

545

550

555

560

565 **Table 3. The proportion of data availability. The percentage represents the proportion of 30 min high-quality EC
data.**

Variable type	SX-cropland		DT-cropland		XZ-suburb		DS-suburb	
	Duration	Proportion	Duration	Proportion	Duration	Proportion	Duration	Proportion
Wind direction		0.99		0.99		0.82		0.92
Wind speed		0.99		0.99		0.82		0.92
Air temperature		0.99		0.99		0.87		0.92
Relative humidity		0.96		0.99		0.87		0.92
Air pressure		0.99		0.99		0.87		0.92
K_d		0.90		0.96		0.67		0.93
K_t	15 Jul 2015– 24 Apr 2019	0.90	1 Dec 2014– 30 Nov 2017	0.96	27 Mar 2014– 22 Jan 2017	0.67	16 Apr 2011– 1 Jan 2019	0.87
L_d		0.90		0.96		0.65		0.75
L_t		0.90		0.96		0.67		0.76
λE		0.71		0.70		0.72		0.76
H		0.87		0.78		0.72		0.80
$G_{0.05}$		0.90		0.96		0.87		0.94
CO ₂		0.73		0.71		0.70		0.82

570

575

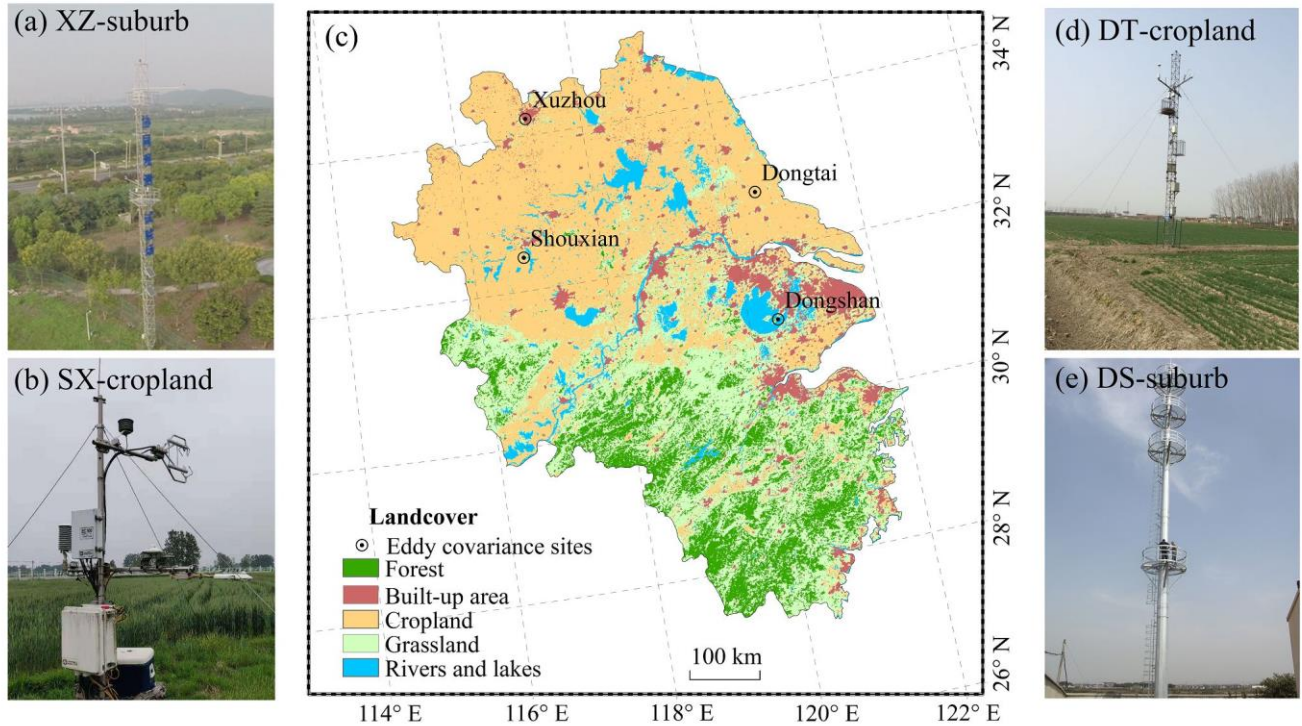
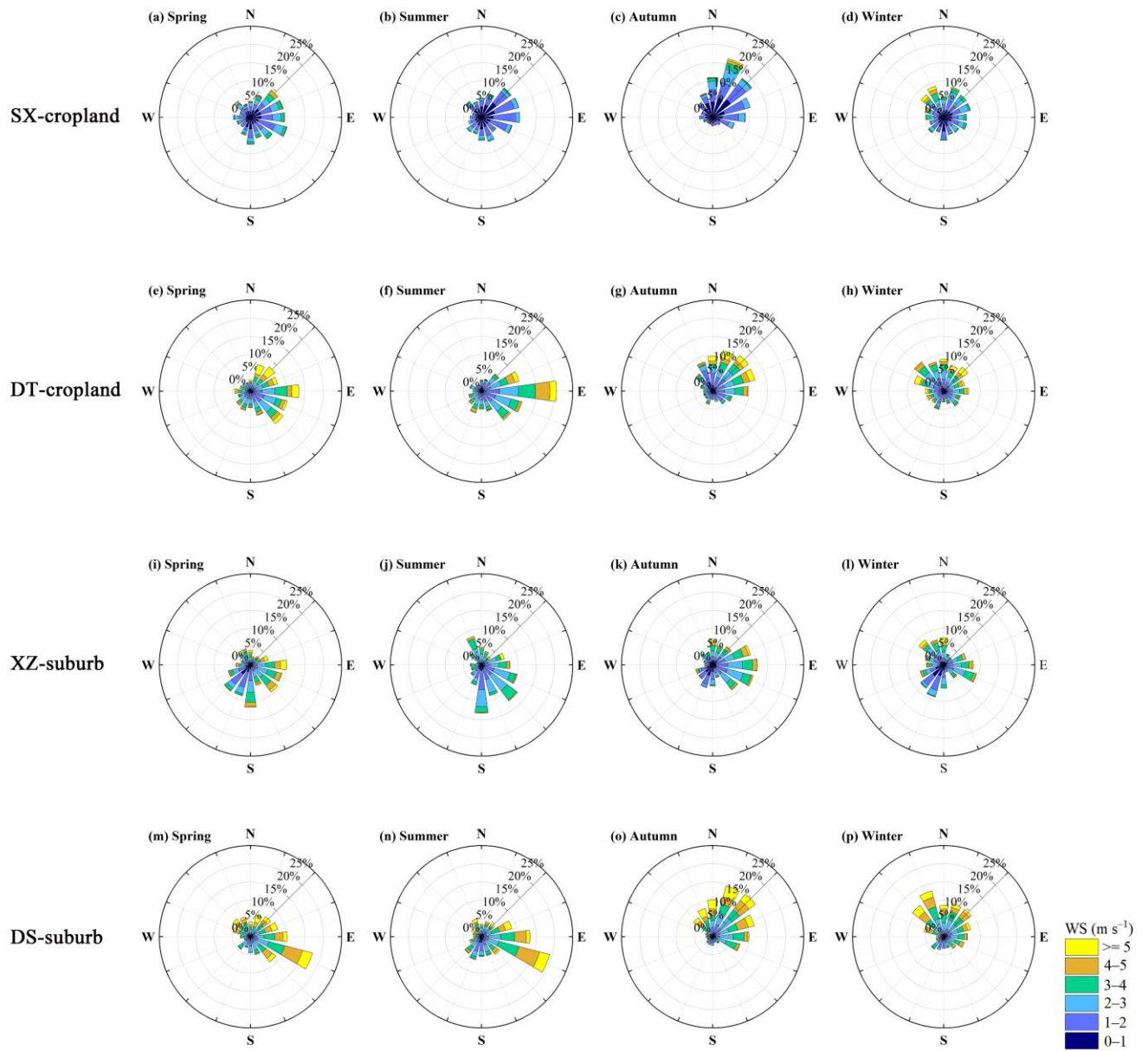


Figure 1: Surface types of the four field sites at (a) XZ-cropland, (b) SX-cropland, (d) DT-suburb, (e) DS-suburb, and (c) the relative position in the Yangtze River Delta of Eastern China. The landcover map in 2016 (c) was available at a 500 m spatial resolution of the MODIS MCD12Q1 product (source: <https://ladsweb.modaps.eosdis.nasa.gov/search/>, last access: 17 August 2022). Flux tower photos in (a), (b), (d), and (e) were taken at the site by ourselves.



585

Figure 2: The seasonal (spring, March–May; summer, June–August; autumn, September–November; and winter, December–February) dynamics of wind roses (22.5° bins, 30 min data) stratified by wind speed frequency for (a)–(d) SX-cropland, (e)–(h) DT-cropland, (i)–(l) XZ-suburb, and (m)–(p) DS-suburb sites.

590

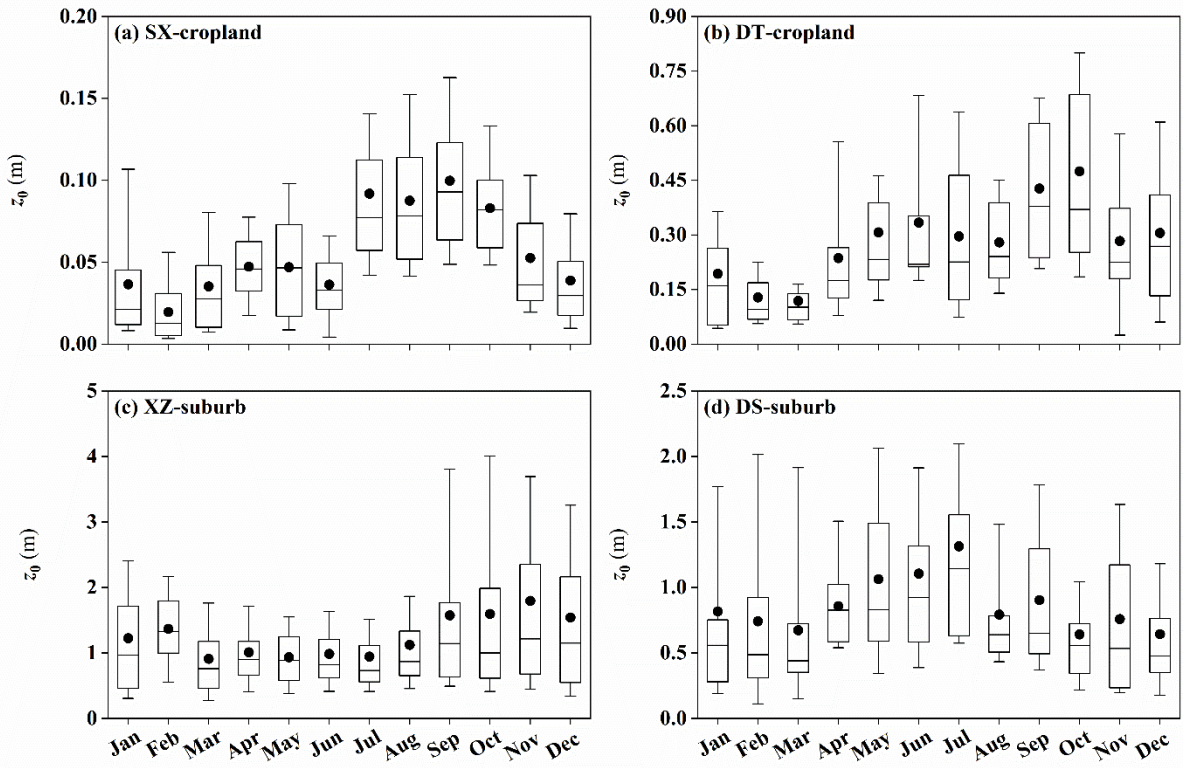


Figure 3: Variations of monthly aerodynamic roughness length (z_0) at (a) SX-cropland, (b) DT-cropland, (c) XZ-suburb, and (d) DS-suburb sites. Boxplots (25, 50 and 75th percentiles) with 10 and 90th percentiles whiskers plus mean (black dot).

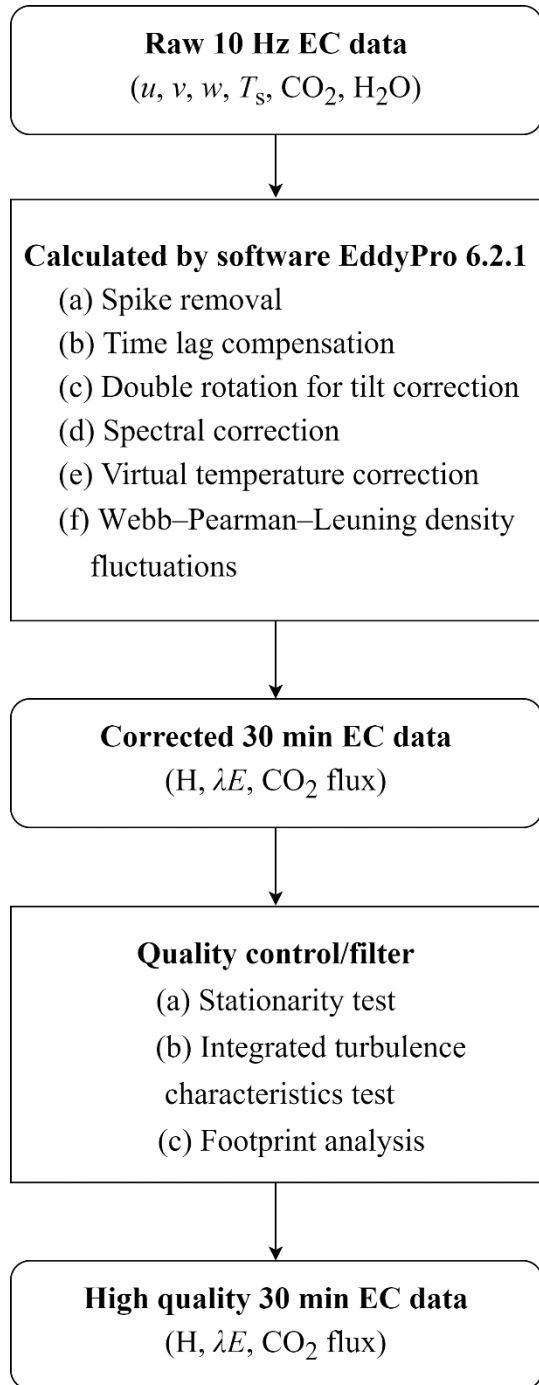


Figure 4: Flowchart of the EC data processing and quality assurance and control.

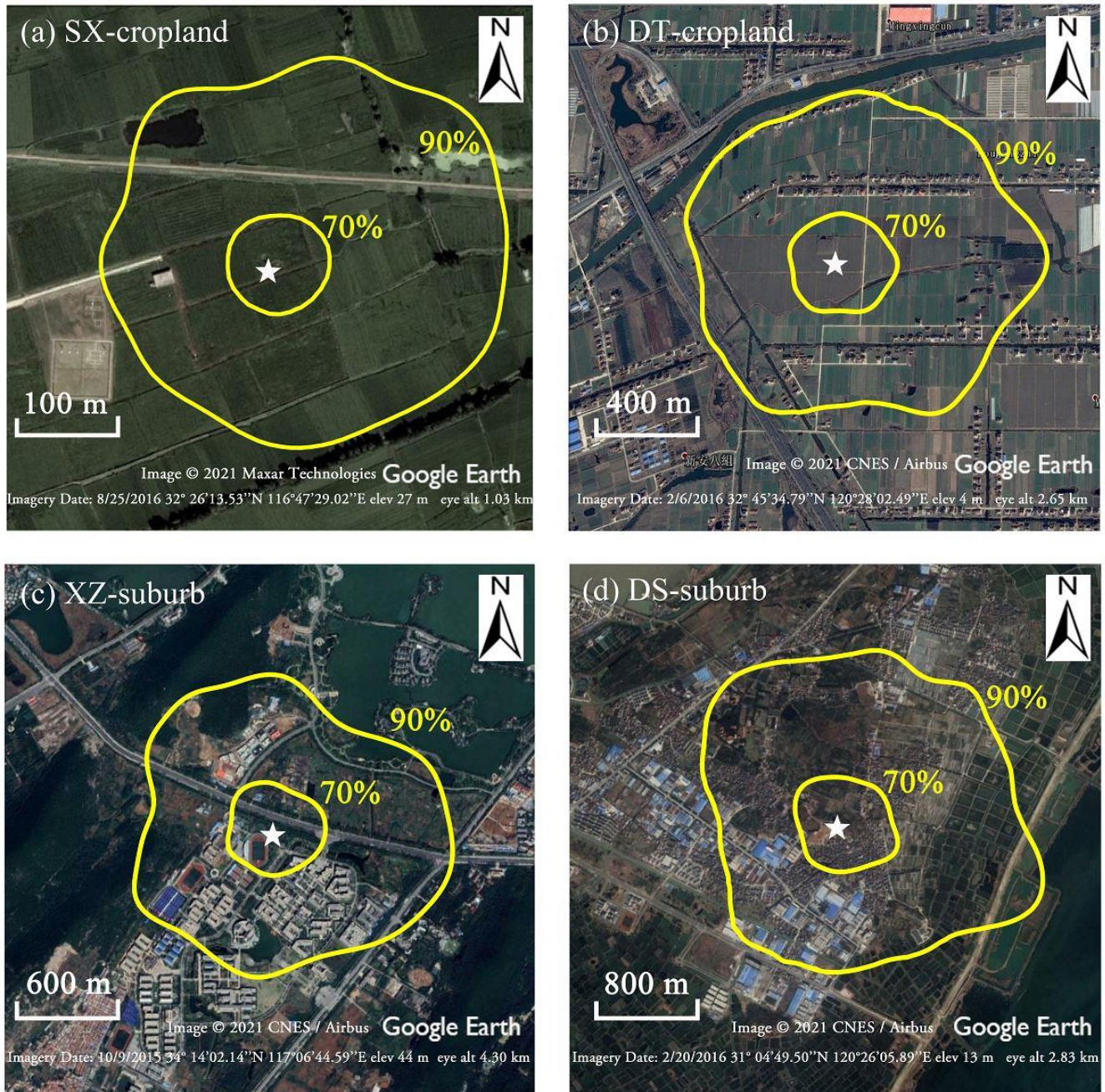
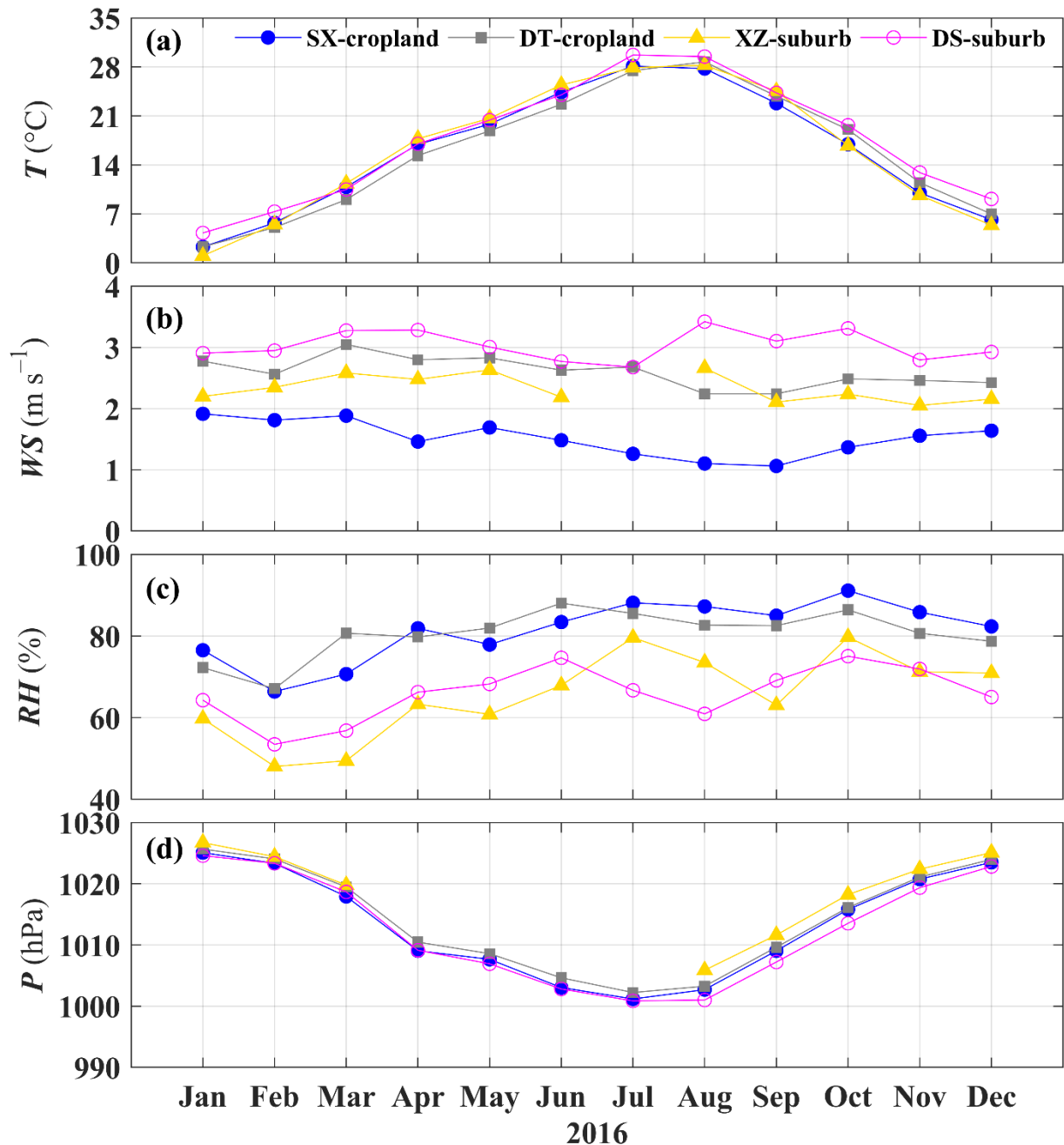


Figure 5: Probable eddy covariance flux source areas (70 % and 90 %, yellow lines from inside to outside) by Kljun et al. (2015) footprint model for (a) SX-cropland, (b) DT-cropland, (c) XZ-suburb, and (d) DS-suburb sites. The white star represents the flux tower location.



605

Figure 6: Monthly mean (a) air temperature (T), (b) wind speed (WS), (c) relative humidity (RH), and (d) air pressure (P).

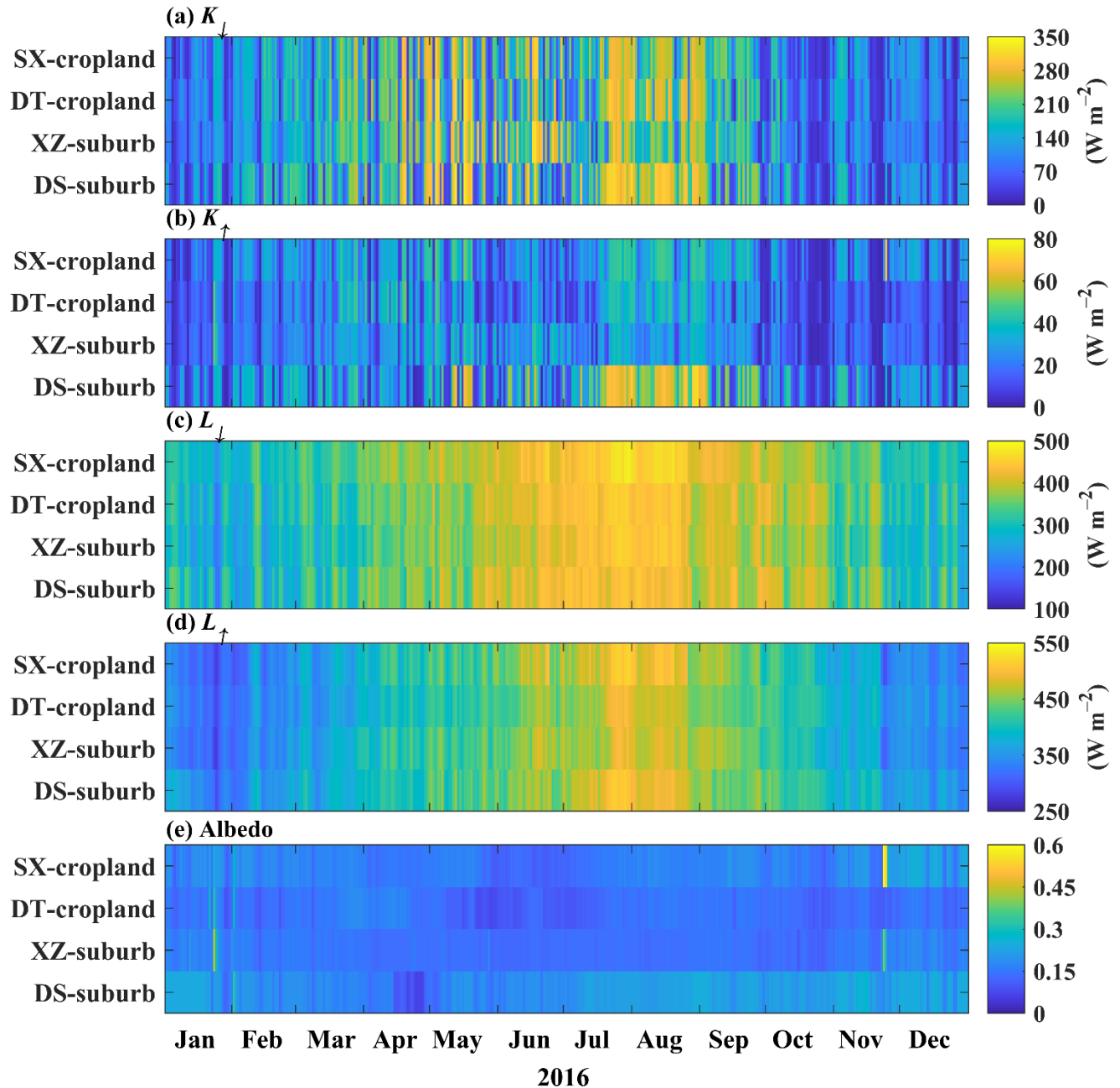
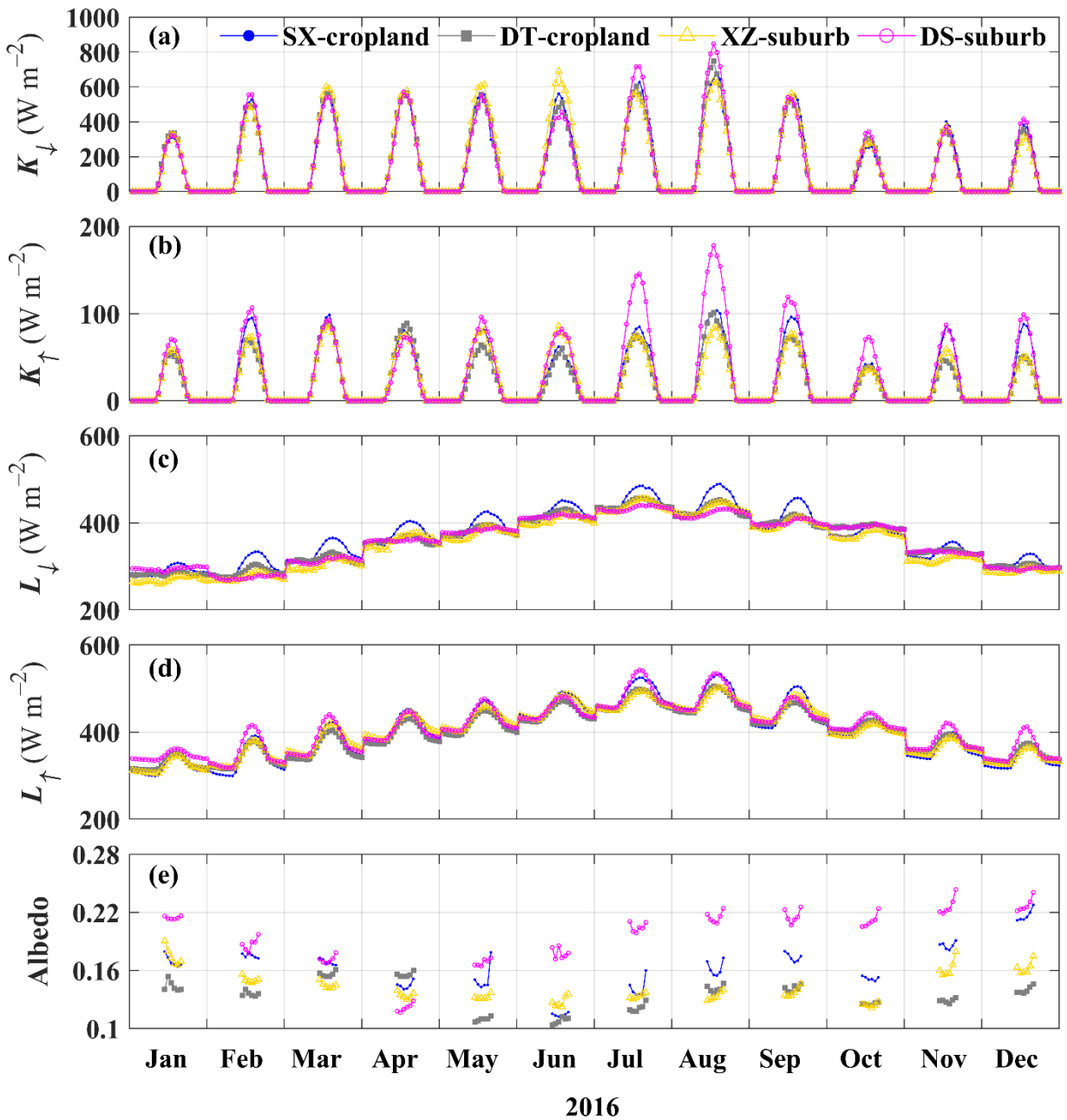


Figure 7: Seasonal variations in daily mean (a) incoming shortwave radiation K_{\downarrow} , (b) outgoing shortwave radiation K_{\uparrow} , (c) incoming longwave radiation L_{\downarrow} , (d) outgoing longwave radiation L_{\uparrow} , and (e) surface albedo.

610



615

Figure 8: Diurnal cycle of the monthly mean (a) incoming shortwave radiation K_{\downarrow} , (b) outgoing shortwave radiation K_{\uparrow} , (c) incoming longwave radiation L_{\downarrow} , (d) outgoing longwave radiation L_{\uparrow} , and (e) surface albedo.

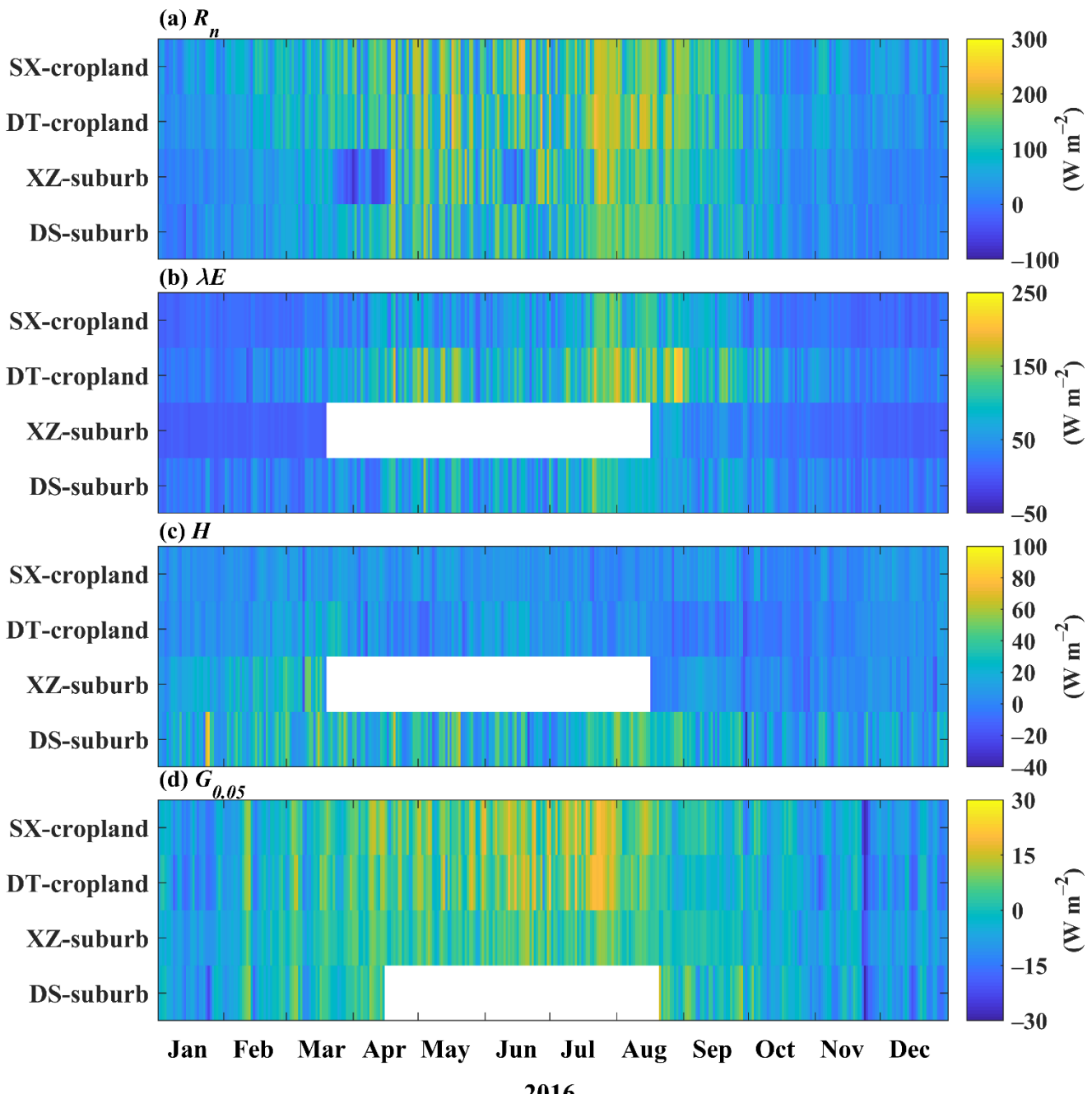


Figure 9: As in Figure 7, but for (a) R_n , (b) λE , (c) H , and (d) $G_{0.05}$.

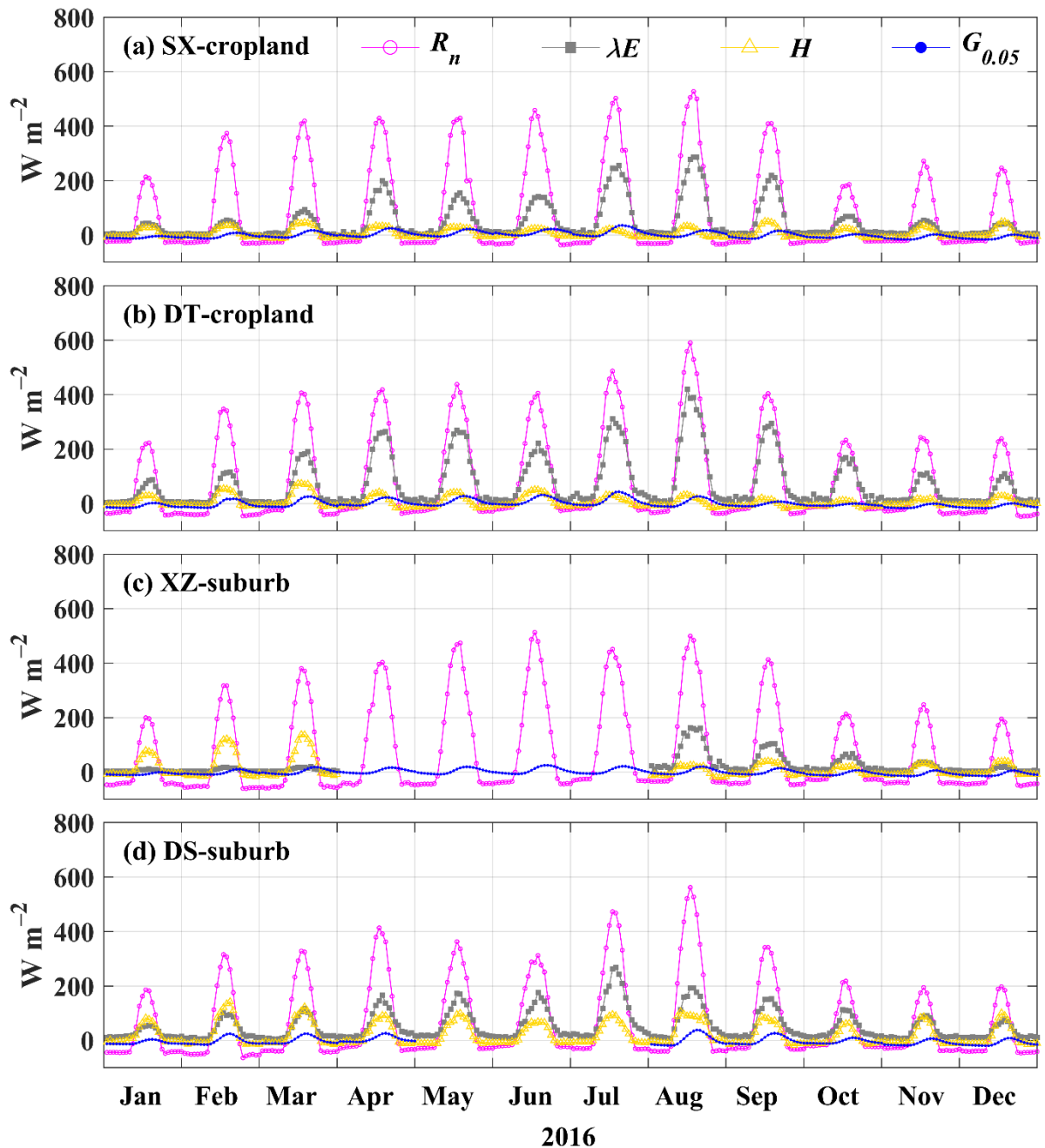


Figure 10: Diurnal cycle of the monthly mean net radiation (R_n), latent heat flux (λE), sensible heat flux (H), and soil heat flux at a depth of 0.05 m ($G_{0.05}$) at (a) SX-cropland, (b) DT-cropland, (c) XZ-suburb, and (d) DS-suburb sites.

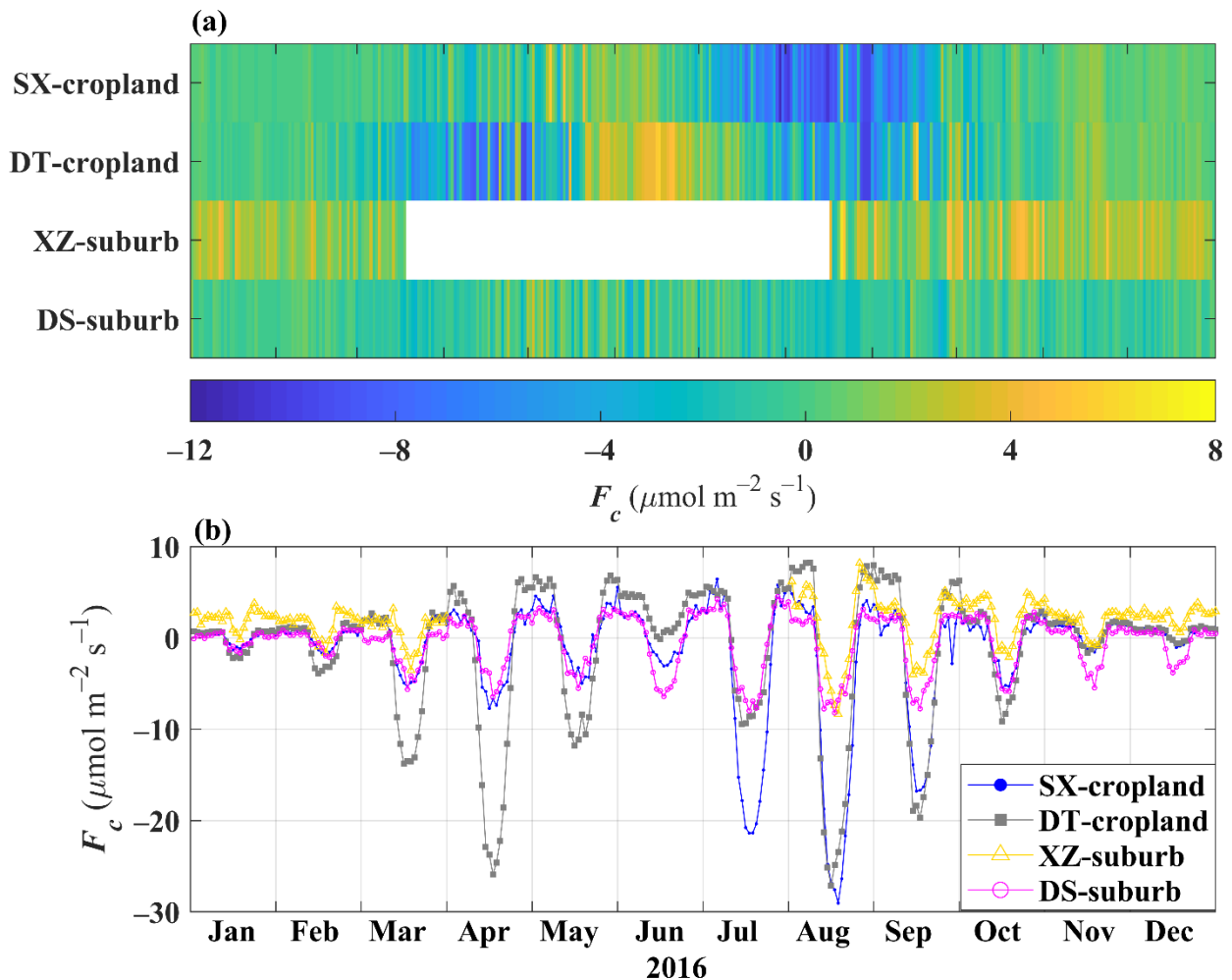


Figure 11: (a) Seasonal and (b) monthly diurnal patterns of CO₂ exchanges in 2016 at four sites.